PAPER

Check for updates

Asymmetric seed passivation for regioselective overgrowth and formation of plasmonic nanobowls†

Zachary J. Woessner,[a] George R. Lewis,[b] Sandra L. A. Bueno,[a] Emilie Ringe [ID] *[b,c] and Sara E. Skrabalak [ID] *[a]

Plasmonic nanoparticles (NPs) have garnered excitement over the past several decades stemming from their unique optoelectronic properties, leading to their use in various sensing applications and theranostics. Symmetry dictates the properties of many nanomaterials, and nanostructures with low, but still defined symmetries, often display markedly different properties compared to their higher symmetry counterparts. While numerous methods are available to manipulate symmetry, surface protecting groups such as polymers are finding use due to their ability to achieve regioselective modification of NP seeds, which can be removed after overgrowth as shown here. Specifically, poly(styrene-*b*-polyacrylic acid) (PSPAA) is used to asymmetrically passivate cubic Au seeds through competition with hexadecyltrimethylammonium bromide (CTAB) ligands. The asymmetric passivation *via* collapsed PSPAA causes only select vertices and faces of the Au cubes to be available for deposition of new material (*i.e.*, Au, Au−Ag alloy, and Au−Pd alloy) during seeded overgrowth. At low metal precursor concentrations, deposition follows observations from unpassivated seeds but with new material growing from only the exposed seed portions. At high metal precursor concentrations, nanobowl-like structures form from interaction between the depositing phase and the passivating PSPAA. Through experiment and simulation, the optoelectronic properties of these nanobowls were probed, finding that the interiors and exteriors of the nanobowls can be functionalized selectively as revealed by surface enhanced Raman spectroscopy (SERS).

Introduction

Seeded nanoparticle (NP) syntheses reliably produce monodisperse NPs with tuneable size, shape, composition, and architecture.[1] Often, seeded syntheses transfer the symmetry of the seeds to the overgrowth product.[2] For example, when using NPs with O_h symmetry as seeds (*e.g.*, cubes, cuboctahedra, and octahedra), our group has reported preservation of seed shape as well as the synthesis of symmetrically branched NPs with O_h symmetry through kinetically controlled overgrowth.[3–6] However, reducing NP symmetry allows for property tuning. In the case of plasmonic nanostructures, the

energies and number of localized surface plasmon resonances (LSPRs) as well as the position of plasmonic hotspots, *i.e.*, regions that provide high E-field enhancement, are symmetry dependent.[7] This idea is captured well by considering the differences between spherical Au NPs, which display one dipolar LSPR mode, and rod-like Au NPs, which display longitudinal and transverse LSPR modes corresponding to the long- and short-axes of the rods.[8]

Here, NPs with high symmetry are asymmetrically capped and used in seeded syntheses to identify how overgrowth processes that typically produce conformal overgrowth or symmetrically branched NPs are modified. As is shown, at low metal precursor concentrations, deposition follows observations from unpassivated seeds but with new material growing only from the seed surfaces not embedded in capping material. In contrast, nanobowls are produced at higher metal precursor concentrations. These observations are explained herein, with this passivation strategy also allowing the interiors and exteriors of the nanobowls to be selectively modified as revealed by surface enhanced Raman scattering (SERS).

Numerous routes toward asymmetric capping of NP seeds have been reported;[9–11] however, unreactive protecting groups

[a] Department of Chemistry, Indiana University – Bloomington, 800 E. Kirkwood Ave., Bloomington, Indiana 47405, USA. E-mail: sskrabal@indiana.edu
[b] Department of Materials Science & Metallurgy, University of Cambridge, 27 Charles Babbage Road, Cambridge, UK, CB3 0FS. E-mail: er407@cam.ac.uk
[c] Department of Earth Sciences, University of Cambridge, Downing Street, Cambridge, UK, CB2 3EQ

are desirable due to their inert interactions with overgrowth solutions and ability to be removed post-overgrowth. Two examples of unreactive protecting groups are silica[12] and collapsed polymers[13–15] (mono- or diblock copolymers) in which the protecting groups can be removed through etching or dissolution. Collapsed polymers are of particular interest due to the ease in which they can be removed. Block copolymers have been studied for this purpose and for their ability to coat NPs in a variety of media through modification of block length and hydrophilicity/hydrophobicity.[16] For example, poly(styrene-*b*-polyacrylic acid) (PSPAA) can uniformly coat both hydrophobic and hydrophilic NPs; however, the addition of a competitive binding ligand led to asymmetric polymer coatings on the NPs.[13] While this method has been shown to produce seeds with restricted surface access, most overgrowth products have been heterodimers (NPs with two phases connected *via* an interface but with both phases exposed to the surface).[15] Thus, investigating other overgrowth chemistries, *e.g.*, conditions that traditionally favour conformal or symmetrically branched overgrowth, with asymmetrically passivated seeds is of interest as such chemistries should allow for regioselective placement of overgrowth material in a predictable manner.

To achieve these goals, PSPAA is used here with the competitive binding ligand hexadecyltrimethylammonium bromide (CTAB) to asymmetrically coat cubic Au NPs (O_h symmetry) with PSPAA shells. These asymmetrically passivated NPs then were used as seeds in reactions which typically lead to conformal coatings or symmetrically branched octopods (*i.e.*, 8-branched NPs with O_h symmetry); however, the asymmetric coating led to regioselective metal deposition on the portions of NP seeds uncoated by PSPAA. The regioselective overgrowth led to half-branched NPs when the amount of overgrowth metal was low, but nanostructures with bowl-like morphologies at a high amount of overgrowth metal. These nanobowls were unexpected but are an exciting development as nanostructures with high curvature are rare on account of their high surface energy. The mechanism for their formation was studied, and dissolution of the PSPAA reveals that the cubic Au NP seeds are centred within the interiors of the nanobowls. The optoelectronic properties of these nanostructures also were explored through both experiment and numerical simulations, in which 3-D tomographic reconstructions of the nanobowls were used directly as models. Notably, the asymmetric capping also allows the interiors and exteriors of the nanobowls to be selectively modified with reporter molecules for SERS.

Experimental

Materials

Chloroauric acid (HAuCl$_4$·3H$_2$O, >99.9%), hexadecyltrimethylammonium bromide (CTAB, BioUltra, >99.5%), cetyltrimethylammonium chloride solution (CTAC, 0.78125 M), ʟ-ascorbic acid (ʟ-aa, 99%), trisodium citrate (>99%), 2-naphthalenethiol (2-NSH, 99%), polyvinylpyrrolidone (PVP, MW 10 000), silver

nitrate (99.9999%), and Pd(ɪɪ) chloride (PdCl$_2$, 99.98%) were purchased from Sigma Aldrich. Sodium bromide (NaBr, 99.50%) was purchased from J.T. Baker. Tetrahydrofuran (THF, ACS grade) was purchased from Macron. Ethanol (anhydrous, ACS grade) was purchased from Pharmco. 4-Mercaptobenzonitrile (4-MBN, 97%) was purchased from Combi-Blocks. Hydrochloric acid (1 M) was purchased from Mallinckrodt. Poly(styrene-*b*-acrylic acid) (*b*-PS = 16 000, *b*-PAA = 3700, PDI = 1.04) was purchased from Polymer Source. Hydrogen tetrachloropalladate (H$_2$PdCl$_4$) was synthesized through the dissolution of Pd(ɪɪ) chloride in 20 mM hydrochloric acid under stirring and mild heat. Nanopure water (18.2 MΩ cm) was used for every experiment.

Methods

Synthesis of Au cubes. Octahedral Au seeds were synthesized using a modified literature protocol[17] and used as seeds for the synthesis of cubic Au NPs. 120 μL trisodium citrate (100 mM) was added to a mixture containing 8.2 mL H$_2$O, 1.5 mL CTAB (100 mM), and 250 μL HAuCl$_4$ (10 mM). The above solution was mixed through gentle swirling and heated in a 110 °C-oil bath overnight. NPs were collected *via* centrifugation (8000 rpm, 15 minutes) and redispersed in 3 mL H$_2$O. Seed concentration was standardized such that a 10 : 1 dilution of the NPs had an absorbance at 400 nm (A_{400}) of 0.14. These NPs were then used as seeds for the synthesis of Au cubes. In short, 1.5 mL ʟ-aa (100 mM) was added to a mixture containing 21.4 mL H$_2$O, 100 μL HAuCl$_4$ (100 mM), and 2 mL CTAB (200 mM) in a 30 mL reaction vial. Directly after, 1.0 mL of octahedral Au seeds from above was added, and the solution was mixed through inversion. The reaction vial was allowed to sit, undisturbed, in a 25 °C-oil bath overnight. NPs were collected *via* centrifugation (8000 rpm, 15 minutes) and redispersed in 3 mL H$_2$O. Au cube concentrations were standardized such that a 10 : 1 dilution had an A_{400} of 0.85 before addition of PSPAA shell.

Synthesis of asymmetrically PSPAA coated cubic Au NPs. A PSPAA shell was grown on cubic Au seeds through mixing 80 μL of PSPAA solution (8 mg mL^{-1} in DMF) with 820 μL DMF. Into this solution was added 130 μL Au NP solution (washed twice to remove excess CTAB) and 70 μL H$_2$O. The vial was mixed through gentle swirling to ensure homogenization. Directly after, 80 μL CTAB (10 mM) was added, followed by quick mixing and placing into a 110 °C oil bath for 2 hours, after which the vial was allowed to slowly cool to room temperature overnight. Asymmetrically coated NPs were collected *via* centrifugation (8000 rpm, 15 min) and washed three times before finally redispersing in 200 μL H$_2$O These NPs were used directly as seeds for the seed-mediated synthesis of mono- and multimetallic branched nanobowls. Note: Asymmetric PSPAA shells are sensitive to CTAB concentration. Conformal coating will be observed if the CTAB concentration is too low, and no coating will be observed if the CTAB concentration is too high. Careful tuning may be necessary for individual systems.

Overgrowth using asymmetrically PSPAA coated cubic Au NP seeds. Overgrowth on the asymmetrically passivated cubic Au

NPs was done using seed-mediated routes. For the Au overgrowth system, a mixture of 2.13 mL nanopure H_2O, 250 μL NaBr (50 mM), 10 μL $HAuCl_4$ (100 mM), and 200 μL CTAC (200 mM) was added to a 2-dram reaction vial. This mixture was mixed through inversion before adding 150 μL of freshly prepared L-aa (100 mM). Directly after, the mixture was gently swirled before adding 100 μL of asymmetrically passivated cubic Au NP seeds. The vial was allowed to sit undisturbed on the benchtop for 4 hours. The NPs were then collected *via* centrifugation (8000 rpm, 15 min) and redispersed in 200 μL nanopure H_2O.

For the Au–Pd overgrowth system, a similar mixture of 2.13 mL nanopure H_2O, 250 μL NaBr (50 mM), 10 μL $HAuCl_4$ (100 mM), 10 μL H_2PdCl_4 (10 mM), and 200 μL CTAC (200 mM) was added to a 2-dram reaction vial. This mixture was mixed through inversion before adding 150 μL of freshly prepared L-aa (100 mM). Directly after, the mixture was gently swirled before adding 100 μL of asymmetrically passivated cubic Au NP seeds. The vial was allowed to sit undisturbed on the benchtop for 4 hours. The NPs were then collected *via* centrifugation (8000 rpm, 15 min) and redispersed in 200 μL nanopure H_2O. For the Au–Ag overgrowth system, a similar method to above was used; however, 10 μL $AgNO_3$ (10 mM) was substituted in place of the 10 μL H_2PdCl_4 (10 mM) above.

Removal of PSPAA shell. The PSPAA shell was removed from the NPs after secondary material was deposited on the asymmetrically PSPAA coated cubic Au NPs. In short, a 100 mM PVP solution was made by dissolving 111.1 mg PVP (MW = 10 000) in 10 mL of THF : EtOH 90 : 10 v/v solution. 100 μL NP solution was dispersed into 1 mL of the PVP solution (note: the mixture of NP and PVP solution should get rather cloudy). The mixture was then centrifuged (8000 rpm, 30 min) to collect the NPs. After decanting the supernatant, the NPs were redispersed in 1 mL PVP solution and then recollected *via* centrifugations. This process was repeated at total of three times to ensure removal of PSPAA. Finally, the particles were redispersed in 100 μL H_2O.

Tomography acquisition and reconstruction details. Data was acquired on an FEI Krios operating at 300 keV. For each sample, we acquired 100 Scanning Transmission Electron Microscopy High Angle Annular Dark-Field (STEM-HAADF) images with steps of 1.5° between ± 60°, and steps of 1° between ± 60° and ± 70°; frames obscured at high angle were manually removed. Image-shift was aligned using a phase correlation algorithm on Sobel-filtered images, and the tilt-axis was aligned using a manual procedure to minimize arcing in the reconstructions. Tomographic reconstruction was performed using a compressed sensing algorithm formulated as in Goris *et al.*[18] with a weighting of 0.05 for the total variation regularization term, implemented with 1000 iterations of a Chambolle–Pock algorithm.[19] Intensity thresholding and segmentation was then carried out in Avizo to produce the final isosurfaces. For the Au@AuAg sample, the seed and overgrowth were separated by intensity values, and a consistent interface was achieved using one iteration of a volume growth algorithm.

Finite-difference time-domain simulations. FDTD numerical simulations were carried out using the Lumerical software, with imported 3D tomographic reconstructions. The dielectric function for Au was fitted to optical data from Johnson and Christy and applied to the 3D tomography reconstruction.[20] The excitation source was a plane wave with a wavelength range of 300–3000 nm propagating through a surrounding medium with refractive index set to 1.3334 to simulate surroundings consistent with water. Mesh values were set to $(4 \text{ nm})^3$ to calculate the scattering cross section and $(1 \text{ nm})^3$ for near-field enhancement maps. E-field enhancement maps were made in Paraview software using the data obtained through Lumerical simulations.

Characterization methods. Scanning electron microscopy (SEM) images were collected on a Zeiss Auriga Focused-Ion Beam (FIB) in SEM mode at a beam energy of 30 kV, an aperture size of 30 μm, and a working distance of 5 mm. Transmission electron microscopy (TEM) images were collected on a JEOL 3200FS TEM operating at 300 kV with a spot size of 1. Energy dispersive X-ray spectroscopy (EDS) was collected using an Oxford Inca dispersive X-ray system interfaced to the JEOL 3200FS TEM operating at 300 kV in STEM mode for single NP elemental analysis. For bulk elemental analysis of multimetallic samples, SEM-EDS was used with the Oxford Inca dispersive X-ray system interfaced to the Zeiss Auriga FIB in SEM mode with an aperture size of 20 μm and working distance of 8 mm. UV-Visible spectroscopy for LSPR measurements was conducted on a Varian CARY 5000 UV-vis-NIR spectrophotometer with a scan rate of 600 nm min^{-1} over a wavelength range of 400–1300 nm. Raman measurements were done using a Horiba XploRA Plus Raman microscope using a 785 nm laser with a 25% intensity filter applied, a 1200 line per mm grating, and a 100× objective lens where data was collected with 5 s acquisition times over 3 accumulations. Enhancement factors were calculated using prior methods (see ESI† for more information).[21] Raman samples were prepared by drop-casting functionalized colloidal NPs onto a silicon substrate. SEM samples were prepared by drop-casting a colloidal suspension (approx. 2 μL solution) on a Si wafer followed by washing with methanol after solvent evaporation. TEM samples were prepared by drop-casting about 2 μL of NP solution onto a chloroform washed 300 mesh carbon-coated copper grid (to remove formvar) and then dried samples were allowed to soak in acetone for at least 24 hours before sample analysis. NP measurements were done using the ImageJ software and taking the mean size of at least 200 NPs *via* SEM images.

Results and discussion

Synthesis and characterization of plasmonic nanobowls

Au cubes (edge length 41 ± 3 nm, Fig. S1†) were synthesized and used to study metal overgrowth on seeds with asymmetric surface passivation. The surface protecting group PSPAA was used, which was demonstrated to conformally coat the cube

surfaces (Fig. S2a†). The PSPAA-coated Au cubes exhibited agglomeration under TEM imaging, which is believed to be an artefact of the sample preparation process. Asymmetric passivation was induced through competitive ligand adsorption *via* the addition of dilute CTAB, which is proposed to disrupt the ability of PSPAA to effectively wet the NP surfaces before collapsing. The cubic seeds were washed twice by centrifugation and redispersion prior to PSPAA additions to ensure minimal residual CTAB presence from the cube synthesis. These conditions, with both PSPAA and CTAB present, led to asymmetrically passivated Au cubes with portions uncoated with polymer (Fig. S2b†). These asymmetrically coated Au cubes were used as seeds in the seed-mediated deposition of Au, Au–Pd, and Au–Ag *via* the reduction of metallic salts ($HAuCl_4$, $HAuCl_4$ and H_2PdCl_4, and $HAuCl_4$ and $AgNO_3$, respectively) by L-ascorbic acid in the presence of cetyltrimethylammonium chloride (CTAC) and NaBr with the overall process and representative products shown in Fig. 1. The reaction conditions for the resulting nanobowl-like particles were selected to mimic reaction conditions that would traditionally lead to conformal overgrowth or symmetrically branched NPs from unpassivated Au seeds, with SEM images of the products from these control experiments shown in Fig. S3.† After growth, the PSPAA surface coating could be removed through dissolution by dispersing the NPs in 100 mM PVP solution in 90 : 10 THF : EtOH

(see Experimental section for further details). The removal of the PSPAA shell left a nanobowl architecture (Au, Au–Pd, and Au–Ag) with the vestige of Au cubes in the centre base of the nanobowls, also depicted schematically in Fig. 1. Interestingly, the bowl-like overgrowth displayed different structural features depending on the metals used in the overgrowth process, with the characterization of each system shown in Fig. 2–4.

When $HAuCl_4$ was reduced by L-aa in the presence of CTAC and NaBr to deposit Au on the asymmetric PSPAA-passivated Au seeds, branching grew along the PSPAA shell, with the portion of the Au cube coated in PSPAA clearly visible in the void present after PSPAA dissolution (Fig. 2). This growth mode will be discussed in more detail later but contrasts with the resulting NPs obtained using unmodified Au cubes as seeds. When all synthetic conditions are maintained except for using unmodified Au cubes as seeds, larger cubic NPs with O_h symmetry (79 ± 7 nm edge length, Fig. S3a†) are produced. Two nanobowls were further analyzed by tilting the SEM stage from 0° to 45° in 15° increments revealing some variance in the degree of cube exposure, *i.e.*, face exposed, edge exposed, or corner exposed (Fig. 2a–d and e–h). This observation is attributed to the stochastic nature of the PSPAA addition to the Au cubes, but the overall archetype of the resulting NP shape (*i.e.*, nanobowl) is maintained regardless of seed exposure. To confirm the general morphology, 3-D STEM
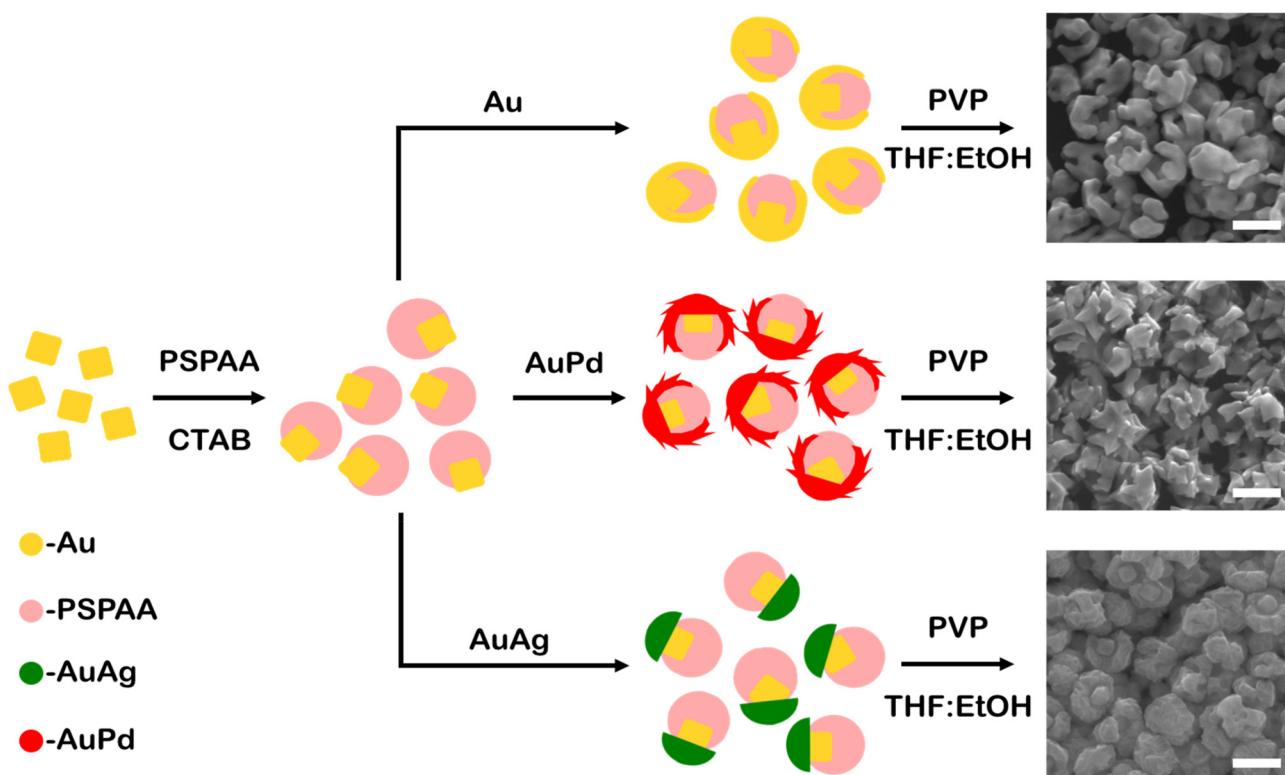

Fig. 1 General scheme for the synthesis of mono- and multi-metallic plasmonic nanobowls from cubic Au seeds where PSPAA is used to asymmetrically passivate Au cubes and metal is allowed to grow on the exposed Au surfaces with Au (top), Au–Pd (middle), and Au–Ag (bottom) systems demonstrated. Afterwards, the PSPAA is removed to expose the interior of the nanobowl, with SEM images of representative products on right. Scale bars 150 nm throughout.
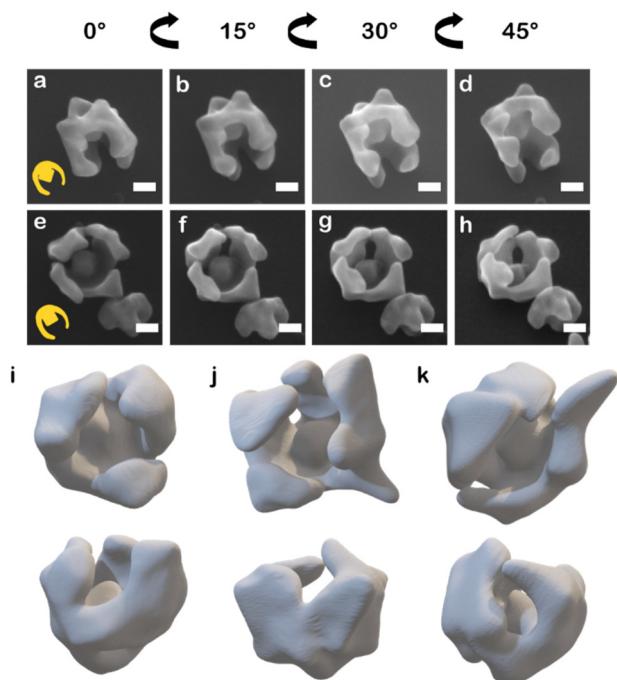
Fig. 2 SEM images of product from Au overgrowth on Au nanocubes with asymmetric PSPAA capping, after PSPAA removal. An example of a cube corner being exposed (a–d) at (a) 0°, (b) 15°, (c) 30°, and (d) 45° tilt and a cube face exposed at (e) 0°, (f) 15°, (g) 30°, and (h) 45° tilt. Sample stage was tilted while keeping the working distance equal for each image. Scale bars 50 nm throughout. 3-D STEM tomographic reconstructions for (i–k) 3 individual nanobowls, looking top-down (upper) and from the side (lower) demonstrating segmented, discontinuous bowl-like morphology.

tomographic reconstructions were acquired for several Au nanobowls (Fig. 2i–k), highlighting the segmented nanobowl growth.

When considering the co-reduction of $HAuCl_4$ and H_2PdCl_4 (input precursor Au : Pd ratio 10 : 1 selected because prior work demonstrated it as optimal for growth of symmetrically branched NPs) by L-aa in the presence of CTAC and NaBr, similar bowl-like NPs to the monometallic system just described were achieved (Fig. 3a–d, 12.6 ± 0.6 at% Pd), but these nanobowls have a more jagged profile. This outcome is in contrast to when this reaction is carried out without the PSPAA shell present, where eight-branched NPs with 11.0 ± 0.3 at% Pd and O_h symmetry are obtained (106 ± 6 nm face diagonal, Fig. S3b†). The presence of Pd, with its higher melting point and lower rate of diffusion on Au likely stabilizes the sharp features present in these structures.[22,23] The composition was analysed by STEM-EDS elemental mapping (Fig. 3e–h) which supports mixing of Au and Pd at the nanoscale. Line scan analysis (Fig. 3i) shows an increase in Au signal at the location of the cubic Au seed.

Interestingly, co-reducing $HAuCl_4$ and $AgNO_3$ (input precursor ratio Au : Ag 10 : 1) in otherwise identical synthetic conditions to the above systems leads to the archetype nanobowl morphology but the bowl is continuous with a rumpled

surface, rather than segmented like the all–Au and Au–Pd systems. This outcome also is in contrast to when co-reduction of Au and Ag precursors is carried out without the presence of the PSPAA shell but otherwise identical conditions. Instead, quasi-spheroidal NPs with a rumpled surface and 7.8 ± 1.6 at% Ag are produced (89 ± 11 nm diameter, Fig. S3c†), demonstrating the necessity of PSPAA to achieving regioselective growth. The continuous yet rumpled morphology is consistent with AuAg deposition on Au nanocubes without PSPAA passivation (Fig. S3†) and likely arises from galvanic replacement of Ag being coupled with the deposition process, although the mechanism has not been studied in detail. The seed position within the bowls show variance in orientation, again reflecting the stochastic nature of PSPAA addition leaving different portions of the cubic Au seeds exposed. For example, tilt study analysis in which the SEM stage was tilted from 0° to 45° at 15° increments for two Au–Ag nanobowls (Fig. 4a–d, 9.4 ± 0.5 at% Ag) show one seed oriented along the C_2 symmetry axis and another seed approximately oriented along the C_4 symmetry axis, consistent with a seed that presumably had an edge and two vertices exposed while the other had an entire face exposed for growth. STEM-EDS elemental mapping supports mixing of Au and Ag at the nanoscale (Fig. 4e–h), where Au and Ag signals are uniformly distributed in the non-cubic portion of the NPs. Performing line scan analysis through a nanobowl oriented with the nanocubic seed in the centre (magenta arrow, Fig. 4i) shows a slight increase in Au signal relative to Ag signal when passing over the seed location. Performing the same analysis on a nanobowl oriented on its side (cyan arrow, Fig. 4j) shows a more significant increase in Au signal relative to Ag signal at the location of the cubic Au seed. To confirm the rumpled nanobowl morphology present in the Au–Ag system, a 3-D STEM tomographic reconstruction was collected (Fig. 4k), demonstrating the cubic features extend from a rumpled bowl. The cubic feature was separated from the overgrowth material *via* intensity values.

Taken together, the presence of the asymmetric PSPAA shell in seed-mediated synthesis allows for regioselectivity in NP overgrowth, resulting in symmetry reduction rather than isotropic overgrowth where symmetry is transferred from seed to resulting NP. However, when beginning this project, the symmetry-reduced structures were anticipated to have some overgrowth domains with similarity to the products obtained from Au nanocubes without PSPAA modification. For example, the rumpled half bowl in the Au–Ag system is similar in texture to the Au–Ag NPs obtained without PSPAA-modified Au seeds. However, in the cases of Au and Au–Pd, the nanobowl morphologies were unexpected. To gain better understanding into the formation of these nanostructures, a concentration study was undertaken. Specifically, the Au–Pd system was selected as the sharp features produced during synthesis are easy to observe. The overall amount of Au precursor added was varied from 2 nmol to 200 nmol while keeping the Au : Pd precursor ratio constant at 10 : 1; for simplicity of discussion, the amount of metal added will be described as a percentage of the maximum amount added. Products were imaged without
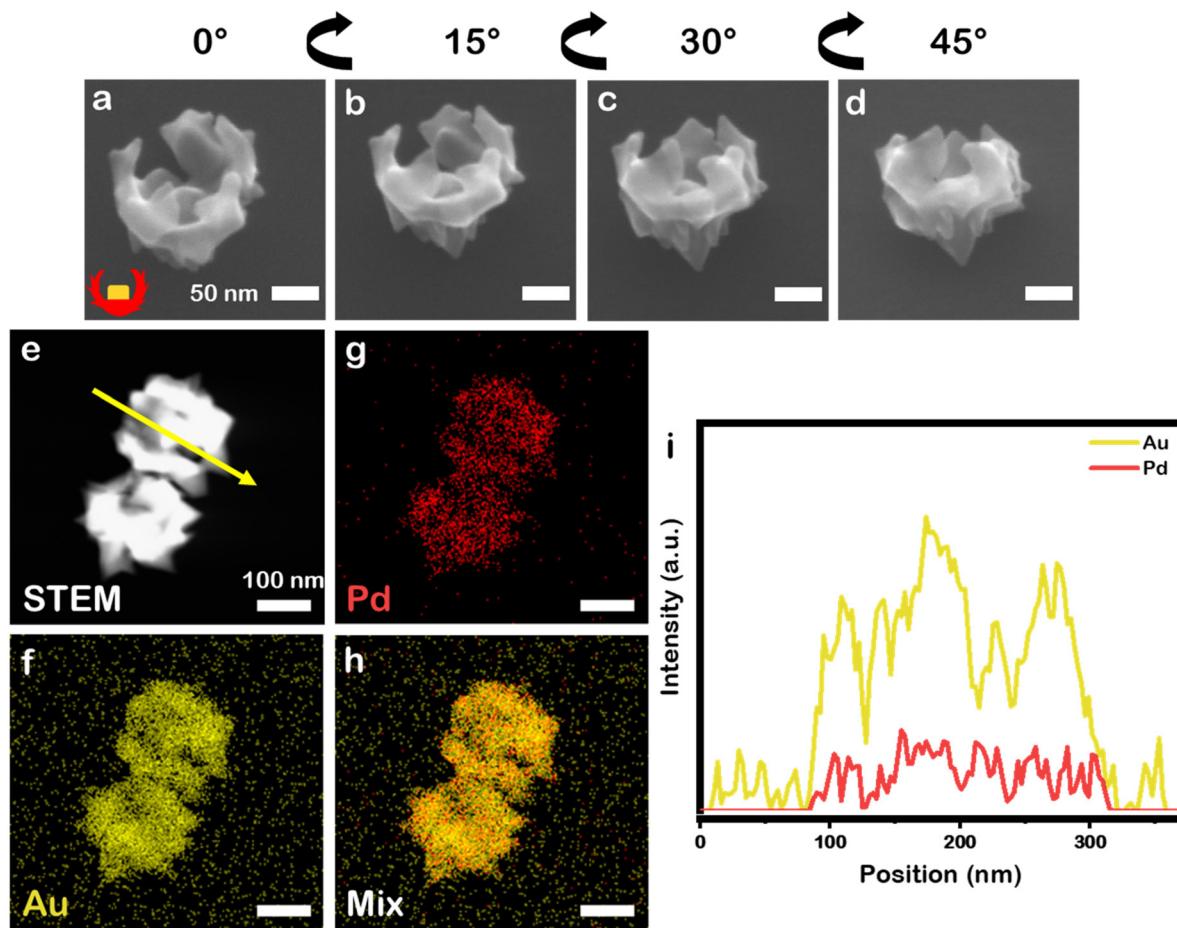
Fig. 3 SEM images of product from Au–Pd overgrowth on cubic Au seeds asymmetrically capped with PSPAA, after PSPAA removal. An example of a cube corner being exposed (a–d) at (a) 0°, (b) 15°, (c) 30°, and (d) 45° tilt after PSPAA dissolution. (e) STEM and (f–h) STEM-EDS elemental maps for (f) Au, (g) Pd, and (h) the overlayed signal. Elemental (i) linescan following the direction of the yellow arrow in (e) demonstrating increase in Au signal in the centre of the particle where the cubic Au seed likely is located. Scale bars 50 nm (a–d) and 100 nm (e–h).

removal of the PSPAA to understand the relationship between added material and the original seed structure.

When co-reducing 1% of the maximum, bright spots are observed in the SEM image at the exposed vertices of the cube (Fig. S4a†). These bright spots indicate overgrowth of material as the exposed vertices of the cube are no longer round, but instead have small protrusions extending away from the cubic seed. Notably, no growth is detected on the PSPAA shell nor new NP formation, indicating the barrier for nucleation is lowest at the high energy sites of the exposed metal seeds. As more material is added (2.5%), the deposition forms more noticeable branches extending from the exposed portion of the cubes (Fig. S4b†) while again no growth is observed on the PSPAA shell. Interestingly, when depositing increasingly more material (5%, 7.5%, and 10%, Fig. S4c–e†), the branches begin to extend and wrap back and onto the PSPAA shell rather than continuing to extend away from the PSPAA shell. This observation suggests that the energetic penalty for creating a new interface by wetting the PSPAA surface is lower than continued growth away from the seed surface. When 25% of the maximum material is deposited, the NP branches extend further around the PSPAA shell (Fig. S4f†). Additionally, the portion of the NP where growth initiated becomes more heavily branched, giving the structure its spiky appearance. Indeed, as more material is added, the trend of branches extending further around the PSPAA shell continues (50%, 100%; Fig. S4g and h,† respectively) until near full encapsulation of the PSPAA shell is achieved. These high metal precursor concentrations (Fig. S4g and h†), also produce Au–Pd octopods through homogeneous nucleation or loss of PSPAA from seeds, but this observation was not studied further. Significantly, the products obtained at low metal precursor content match with expectations from overgrowth from Au nanocubes without PSPAA, where metal deposition occurs preferentially at seed vertices under kinetically controlled overgrowth and more conformal overgrowth would be anticipated with Au nanospheres as seeds. This finding provides predictability on how overgrowth from seeds with regioselective modifications will proceed, where deviations are most likely at conditions of high supersaturation.
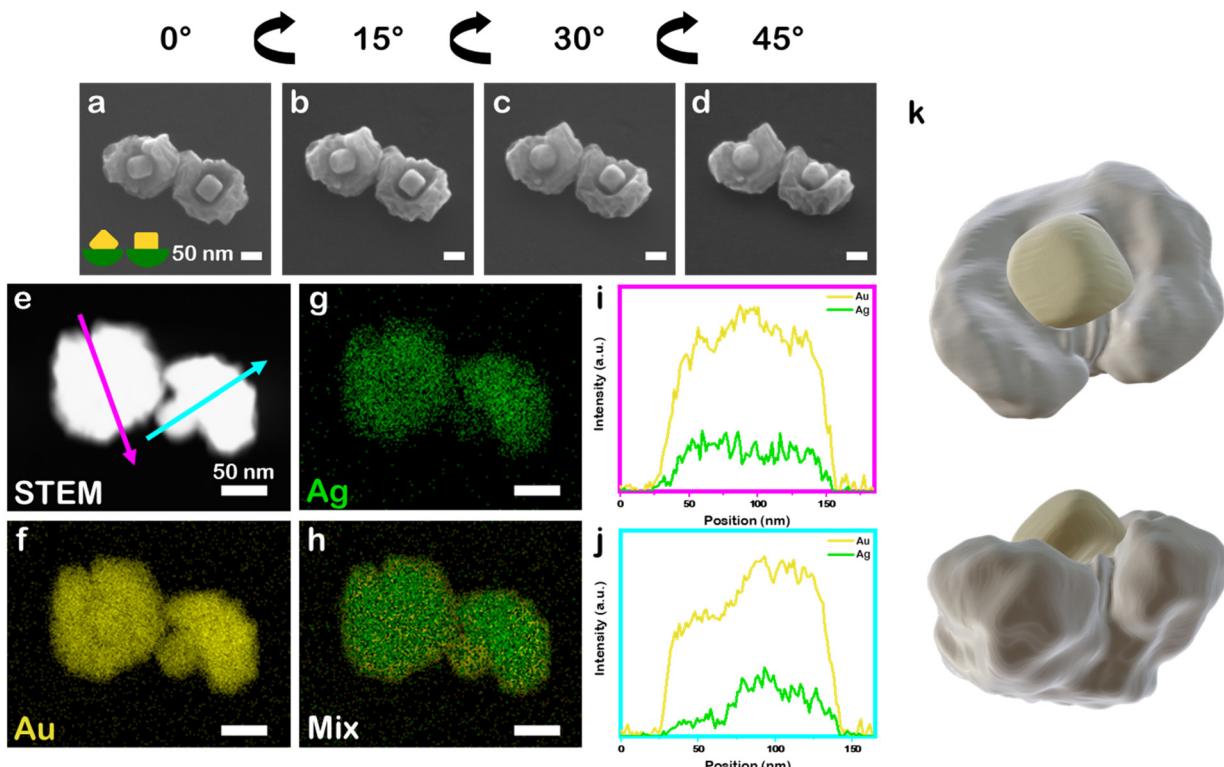
Fig. 4 SEM images of product from Au–Ag overgrowth on cubic Au seeds with asymmetric PSPAA capping, after PSPAA removal. Examples of a two overgrown NPs at (a) 0°, (b) 15°, (c) 30°, and (d) 45° tilt after PSPAA dissolution. (e) STEM and (f–h) STEM-EDS elemental maps for (f) Au, (g) Ag, and (h) the overlayed signal. Elemental linescans following the direction of the (i) magenta and (j) cyan arrows in (e) demonstrating increase in Au signal in the centre of the particle where the cubic Au seed likely is. (k) 3-D STEM tomographic reconstruction for the Au–Ag nanobowl with view from top-down (upper) and from the side (lower) where yellow represents the Au cube portion and grey represents the Au–Ag portion. The different coloured portions were obtained through separating the seed and overgrowth by intensity levels, and a consistent interface was obtained through using a single iteration of a volume growth algorithm.

While deposition kinetics play a role in the overgrowth behaviour, the PSPAA surface charge also likely contributes. The typical pH for the seed-mediated reduction and seed-mediated co-reduction syntheses employed here (~3 for the synthesis of Au–Pd octopods, for which the reactions presented herein had similar conditions)[24] is below the pKa of PSPAA (~4.5 for the PAA block).[25] As the pH of the reaction media is below that of the block copolymer pKa, the acrylic acid portion of the block copolymer is protonated. Such conditions support wrapping of overgrowth material around the PSPAA shell. Interestingly, work by Klupp Taylor *et al.* showed the effect of metal precursor concentration and seed particle concentration on the growth of Au patches on polystyrene seeds, with dendritic patches occurring at both low Au and PS seed concentration and dense protrusions growing away from the PS seed surface occurring at both high Au and PS seed concentration.[26] This switch between growth along the polymer surface to growth away from the polymer surface is fascinating, and may be possible in our system with further study.

Optoelectronic properties of plasmonic nanobowls

Each nanobowl sample displays unique optical properties (Fig. S5†). This finding is unsurprising as both NP compo-sition and shape have been shown to influence plasmonic properties.[27,28] In the case of composition, alloy Au–Ag spheres with a 1 : 1 Au : Ag ratio have a blue-shifted LSPR maximum of approximately 60 nm compared to monometallic Au sphere counterparts.[29] Alloy Au–Pd nanodisks of varying Au : Pd ratios have shown that even at low Pd ratios (Au : Pd ratio 0.9 : 0.1) the dielectric behaviour of the Au–Pd alloy is dominated by Pd contributions; thus, the Au–Pd LSPR is expected to be significantly broadened due to the high imaginary component of the Pd dielectric function.[30] In the case of shape, anisotropic features red shift the LSPR maximum compared to structures without anisotropic features;[31,32] similarly, changes to NP symmetry allows for different dipolar LSPR modes to occur (consider the difference between Au spheres and Au rods).[8,33] Here, the Au nanobowl has the most blue-shifted LSPR (Fig. S5†). Interestingly, the sharp, branch-like features present in the Au–Pd nanobowl system leads to the largest red-shift in LSPR maximum compared to the other nanobowls (811 nm compared to 674 nm and 664 nm for the Au–Ag and Au nanobowls, respectively). The Au–Pd nanobowl also has the broadest LSPR compared to the Au and Au–Ag nanobowls. The incorporation of Pd coupled with the sharp, anisotropic features in the branches in the Au–Pd nanobowl

system leads to both the broadening of the LSPR band and the red-shifted LSPR. Each overgrowth shares a common feature in the LSPR of a defined shoulder peak at roughly 560 nm, likely corresponding to the cube-like features still present in the NPs.

To investigate further the optical properties of these nanobowl systems, the 3D STEM tomographic reconstructions were input directly as models for finite-difference time-domain (FDTD) numerical simulations. For ease of simulation requirements, the Au-only system was selected as a case study to elucidate the far- and near-field optoelectronic properties. When simulating the NP scattering of the reconstructed model (Fig. 5a) through FDTD simulations, several distinct scattering peaks are notable for the model (Fig. 5b) that are not present in the experimental data (Fig. S5,† black trace). This notable difference between experimental and simulated scattering profiles is explained through ensemble effects,[34] which in the case of Au nanostars has shown to give a broad ensemble extinction that differs greatly from single NP measurements.[35] Indeed, while the archetype of nanobowl is consistent throughout the sample, there is a degree of randomness to the samples in terms of branch size and distributions, as indicated from the three unique Au nanobowl reconstructions. This randomness in branching, coupled with the random orientation of NPs in solutions, leads to the single, broad LSPR feature for the experimental extinction rather than distinct LSPR peaks seen in the simulated scattering cross section for single particles. It is notable, however, that most of the scattering peaks found in the reconstruction simulation fall within the broad feature of the experimental system. As such, to account for random motion of the NPs in solution, each

nanobowl model was rotated at 45° increments along the x-, y-, and z-axes from 0° to 180°, providing unique scattering intensities at each orientation (Fig. S6†). These unique scattering intensities were averaged with equal weighting as no orientation would have preference in solution, providing the scattering profile found in Fig. 5.[36]

As there are clearly defined scattering peaks in the simulated data, the near-field E-field enhancements for each wavelength corresponding to a peak in the simulated scattering cross section were simulated (Fig. 5c–e). These near-field simulations provide insights into hotspots present in this class of NP. As NP orientation with respect to the incoming light wave impacts the intensity of scattering of the different peaks, the NP orientation that scattered the strongest at each individual peak in the simulated average was selected and used in the near-field simulation for that wavelength. Interestingly, each orientation demonstrated that the hotspots present in the nanobowl morphology are on the exterior of the nanobowl rather than on the interior. The implications for these E-field distributions will be discussed further below. The lack of strong E-field enhancement on the interior of the nanobowl likely is due to the large void present on the interior of the nanobowl, which presents no features with a small radius of curvature. This finding was consistent with the other Au nanobowl reconstructions used as models (Fig. S7a and b†).

The presence of numerous regions with near-field enhancements indicates the promise of this class of NP for SERS. To best connect experiment to simulation, the Au overgrowth NPs were selected as a case study for SERS measurements. Additionally, to elucidate the enhancements provided by the interior and the exterior of the nanobowl morphology, thiol markers 2-naphthalenethiol (2-NSH) and 4-mercaptobenzonitrile (4-MBN) were selected due to distinct Raman scattering profiles for each Raman marker.[37] That is, 2-NSH has a distinct Raman feature at 1377 cm^{-1} associated with ring breathing[38] and 4-MBN has a distinct Raman feature at 2225 cm^{-1} corresponding to nitrile stretching.[39] The exteriors of the NPs were saturated with Raman marker prior to the removal of the PSPAA coating the interior. After the removal of PSPAA from the interior of the nanobowls, more Raman marker was added to saturate the interior of the NPs. The notation used herein will be A@B where A coats the interior of the nanobowl and B coats the exterior of the nanobowl. The following mixed-thiol systems were studied: 2-NSH on both the interior and exterior (2-NSH@2-NSH), 2-NSH on the interior and 4-MBN on the exterior (2-NSH@4-MBN), 4-MBN on the interior and 2-NSH on the exterior (4-MBN@2-NSH), and 4-MBN on both the interior and exterior (4-MBN@4-MBN).

Unsurprisingly, 2-NSH@2-NSH (Fig. 6a, black trace) had the greatest intensity at 1377 cm^{-1} and 4-MBN@4-MBN (Fig. 6b, green trace) had the greatest intensity at 2225 cm^{-1}. This large intensity for the respective Raman markers is due to the entire surface area of the NPs being coated by only their corresponding thiol marker molecules, leading to enhancement factors (EFs) of 7.7×10^6 and 9.9×10^5 for 2-NSH and 4-MBN, respectively. Interestingly, when considering 2-NSH@4-MBN
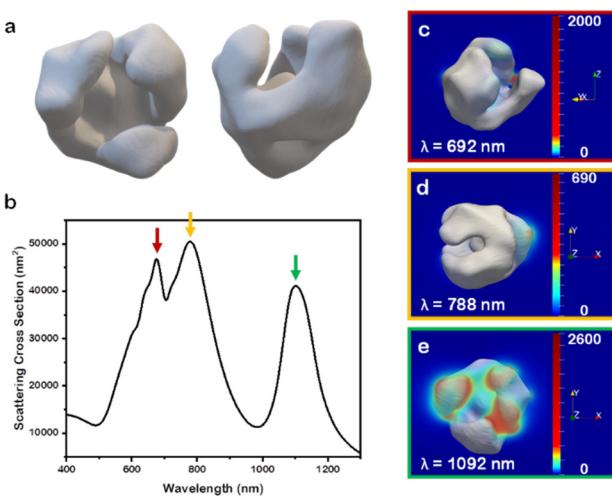

Fig. 5 3D STEM tomographic reconstructions from the (a, left) top down and (a, right) side. (b) Average far-field scattering profile for the model shown in (a) where the model was rotated at 45° increments along the x-, y-, and z-axes from 0° to 180° while keeping the propagation of the light source static along the z-axis. Near-field enhancement maps at each orientation producing maximum scattering in the far-field scattering at (c) 692 nm, (d) 788 nm, and (e) 1092 nm. Source propagated along the z-axis in each simulation.
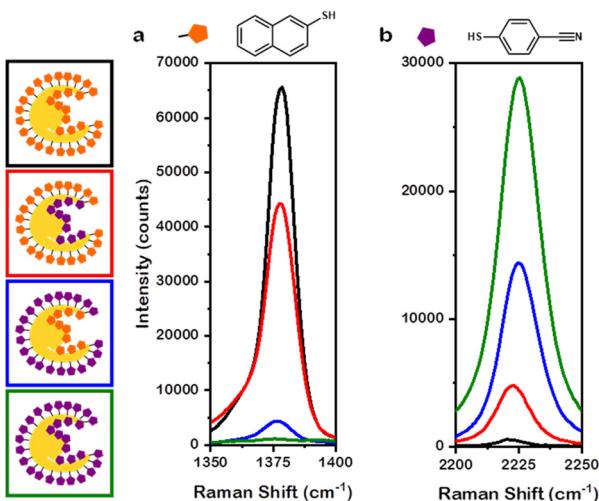
Fig. 6 SERS profiles highlighting (a) 2-NSH and (b) 4-MBN spectroscopic regions of importance for 2-NSH@2-NSH (black trace), 4-MBN@2-NSH (red trace), 2-NSH@4-MBN (blue trace), and 4-MBN@4-MBN (green trace). For corresponding graphics, orange functional group is 2-NSH, and purple functional group is 4-MBN. Data collected on samples drop-cast onto polished Si wafer.

and 4-MBN@2-NSH, the Raman marker coating the exterior of the nanobowls exhibited a higher intensity enhancement compared to the intensity enhancement of the Raman marker coating the interior. For 2-NSH, the EF when the molecules coated the exterior only was 5.2×10^6 while the interior coating was 5.1×10^5. When considering 4-MBN, a less bulky molecule, the EFs were 4.9×10^5 and 1.5×10^5 for the exterior and interior coatings, respectively. As this discrepancy could be due to the difference in the surface area between the exterior and interior of the nanobowls, the EFs for the above systems were normalized by dividing the enhancement factor by the approximate number of Raman markers saturating each samples surface. The saturation conditions were found *via* titration of the same concentration of NPs with thiol marker, see Experimental section for details.

When normalizing the data in this way, 2-NSH and 4-MBN exhibited differences in the interior and exterior EFs. For the case of 2-NSH, the EF on the exterior was 4.3×10^{-9} per molecule while the EF for the interior was 1.1×10^{-9} per molecule. The difference between EF on the interior *versus* the exterior can be understood when considering the roughly 3-fold increase in the number of molecules present on the exterior compared to the interior in addition to the insights provided *via* near-field enhancement plots showing hotspot generation confined to the exterior of the nanobowls. For 4-MBN, interestingly, similar EFs of 4.1×10^{-10} per molecule and 3.3×10^{-10} per molecule were determined for the exterior and interior, respectively. These similar EFs comparing the difference coatings demonstrate greater enhancement for 4-MBN on the interior compared to the enhancement of 2-NSH. The likely reason behind this is the less bulky 4-MBN molecules can pack into the finer features of the interior of the nanobowls

better than can 2-NSH; however, for both molecules, the hotspots generated on the exterior of the nanobowl provide the larger enhancement. The increased enhancement found for the exterior is likely due to the complex morphology, with the non-smooth surface providing opportunities for hotspot generation on the exterior; however, the large distance between the cube and the NP interior walls is unfavourable for hotspot generation. Thus, larger enhancements per molecule are observed on the exterior than for the interior.

Taken together, as the hotspots for these NPs were found to occur on the exterior of the nanobowl through simulation, the larger EF for the thiol molecules coating the exterior is reasonable. Thus, the EF for the exterior is contributed to by both the larger surface area providing a platform for more molecules to adsorb and the presence of hotspots on the surface leading to larger enhancements. For increasing the likelihood of generating hotspots on the interior of the nanobowl, future NP design should be for structures that either have a smaller void present in the interior of the nanobowl (through smaller PSPAA shells) or through using branched NPs as seeds for adding sharp, anisotropic features to the interior. For example, concave Au–Pd NPs with O_h symmetry (*i.e.*, octopods) could be used as seeds for the asymmetric additions of PSPAA protecting moieties. These asymmetrically passivated Au–Pd NPs were used as model seeds for demonstrating the synthesis of nanobowls with a branched NP interior. For ease of visualization, the Au–Ag nanobowl system was used to demonstrate a rumpled Au–Ag nanobowl with a branched Au–Pd interior (Fig. S8†). Taken together, these plasmonic nanobowls provide unique platforms for complex SERS sensors with a tuneable interior and exterior morphology through fine-tuning the synthetic design parameters such as reaction conditions, precursor selection, and seed shape.

Conclusions

In summary, cubic Au NPs were asymmetrically coated with PSPAA through competitive binding interactions with CTAB. These asymmetrically passivated Au cubes were used as seeds to understand how the use of these protecting groups can be used to achieve regioselective modification of NPs. Notably, at low metal precursor concentrations, overgrowth followed behaviour observed with non-passivated seeds just on the metal exposed portions, making regioselective modification of seeds predictable. At high metal precursor concentrations, new nanobowl morphologies were achieved. While the Au and Au–Pd overgrowths displayed discontinuous, segmented bowl-like morphologies guided by the PSPAA, the Au–Ag overgrowth showed a rumpled nanobowl morphology reminiscent of the product obtained from Au cubes without PSPAA passivation.

FDTD simulations of the near- and far-field optoelectronic properties supported hotspot generation along the exterior and edges of the nanobowls rather than their interiors. These hotspots, coupled with the greater surface area of the exterior, led to EFs that were greater for molecules coating the exterior

rather than the interior. Interestingly, smaller, less sterically bulky molecules had nearly equal EFs between the interior and exterior, likely due to better packing efficiency into the finer features of the interior. These plasmonic nanobowls provide interesting platforms for multifunctional SERS substrates with both interior and exterior modularity, where we envision expanding the synthetic library of nanobowls through interior design achieved by seed selection.

Author contributions

S. E. S. and E. R. were responsible for design of experiments. Z. J. W. developed synthesis of cubic seeds, asymmetric polymer passivation strategies, overgrowth steps, optoelectronic characterization, Raman collection, and FDTD numerical simulations. G. R. L. and E. R. were responsible for 3-D STEM tomography experiments and reconstructions of Au and Au–Ag nanobowls. S. L. A. B. assisted with elemental characterization *via* STEM-EDS maps. This manuscript was written through contributions of all authors. All authors have given approval to the final version of this Manuscript.

Conflicts of interest

The authors declare no competing financial interest.

Acknowledgements

References

1 Y. Xia, K. D. Gilroy, H.-C. Peng and X. Xia, *Angew. Chem., Int. Ed.*, 2017, **56**, 60.

2 S. E. Skrabalak, *Acc. Mater. Res.*, 2021, **2**, 621.

3 C. J. DeSantis and S. E. Skrabalak, *Langmuir*, 2012, **28**, 9055.

4 C. J. DeSantis and S. E. Skrabalak, *J. Am. Chem. Soc.*, 2013, **135**, 10.

5 R. G. Weiner, M. R. Kunz and S. E. Skrabalak, *Acc. Chem. Res.*, 2015, **48**, 2688.

6 J. D. Smith, Z. J. Woessner and S. E. Skrabalak, *J. Phys. Chem. C*, 2019, **123**, 18113.

7 K.-Q. Lin, J. Yi, S. Hu, B.-J. Liu, J.-Y. Liu, X. Wang and B. Ren, *J. Phys. Chem. C*, 2016, **120**, 20806.

8 H. Chen, L. Shao, Q. Li and J. Wang, *Chem. Soc. Rev.*, 2013, **42**, 2679.

9 K. D. Gilroy, H.-C. Peng, X. Yang, A. Ruditskiy and Y. Xia, *Chem. Commun.*, 2017, **53**, 4530.

10 Z. Huang, J. Gong and Z. Nie, *Acc. Chem. Res.*, 2019, **52**, 1125.

11 Z. J. Woessner and S. E. Skrabalak, *J. Phys. Chem. C*, 2021, **125**, 23587.

12 T. Chen, G. Chen, S. Xing, T. Wu and H. Chen, *Chem. Mater.*, 2010, **22**, 3826.

13 S. Feng, X. Song, Q. Xu, X. Shen, J. Xu and H. Chen, *J. Phys. Chem. Solids*, 2019, **135**, 109019.

14 Z. Wang, B. He, G. Xu, G. Wang, J. Wang, Y. Feng, D. Su, B. Chen, H. Li, Z. Wu, H. Zhang, L. Shao and H. Chen, *Nat. Commun.*, 2018, **9**, 563.

15 J. Qiu, M. Xie, Z. Lyu, K. D. Gilroy, H. Liu and Y. Xia, *Nano Lett.*, 2019, **19**, 6703.

16 T. Chen, M. Yang, X. Wang, L. H. Tan and H. Chen, *J. Am. Chem. Soc.*, 2008, **130**, 11858.

17 C.-C. Chang, H.-L. Wu, C.-H. Kuo and M. H. Huang, *Chem. Mater.*, 2008, **20**, 7570.

18 B. Goris, W. Van den Broek, K. J. Batenburg, H. Heidari Mezerji and S. Bals, *Ultramicroscopy*, 2012, **113**, 120.

19 A. Chambolle and T. Pock, *J. Math. Imaging Vision*, 2011, **40**, 120.

20 P. B. Johnson and R. W. Christy, *Phys. Rev. B: Solid State*, 1972, **6**, 4370.

21 S. Yoo, J. Lee, J. Kim, J.-M. Kim, M. Haddadnezhad, S. Lee, S. Choi, D. Park, J.-M. Nam and S. Park, *J. Am. Chem. Soc.*, 2020, **142**, 12341.

22 W. Albrecht, E. Bladt, H. Vanrompay, J. D. Smith, S. E. Skrabalak and S. Bals, *ACS Nano*, 2019, **13**, 6522.

23 M. Quintanilla, C. Kuttner, J. D. Smith, A. Seifert, S. E. Skrabalak and L. M. Liz-Marzán, *Nanoscale*, 2019, **11**, 19561.

24 C. J. DeSantis, A. C. Sue, M. M. Bower and S. E. Skrabalak, *ACS Nano*, 2012, **6**, 2617.

25 M. Wiśniewska, T. Urban, E. Grządka, V. Zarko and V. M. Gun'ko, *Colloid Polym. Sci.*, 2014, **292**, 699.

26 T. Meincke and R. N. Klupp Taylor, *Particuology*, 2023, **75**, 137.

27 K. A. Willets and R. P. Van Duyne, *Annu. Rev. Phys. Chem.*, 2007, **58**, 267.

28 H. Chen, X. Kou, Z. Yang, W. Ni and J. Wang, *Langmuir*, 2008, **24**, 5233.

29 S. Link, Z. L. Wang and M. A. El-Sayed, *J. Phys. Chem. B*, 1999, **103**, 3529.

30 S. Kadkhodazadeh, F. A. A. Nugroho, C. Langhammer, M. Beleggia and J. B. Wagner, *ACS Photonics*, 2019, **6**, 779.

31 A. F. Smith, R. G. Weiner, M. M. Bower, B. Dragnea and S. E. Skrabalak, *J. Phys. Chem. C*, 2015, **119**, 22114.

32 J. Cai, V. Raghavan, Y. J. Bai, M. H. Zhou, X. L. Liu, C. Y. Liao, P. Ma, L. Shi, P. Dockery, I. Keogh, H. M. Fan and M. Olivo, *J. Mater. Chem. B*, 2015, **3**, 7377.

33 A. F. Smith, R. G. Weiner and S. E. Skrabalak, *J. Phys. Chem. C*, 2016, **120**, 20563.

34 L. J. Sherry, S.-H. Chang, G. C. Schatz, R. P. Van Duyne, B. J. Wiley and Y. Xia, *Nano Lett.*, 2005, **5**, 2034.

35 K. M. Mayer and J. H. Hafner, *Chem. Rev.*, 2011, **111**, 3828.

36 H.-E. Lee, H.-Y. Ahn, J. Mun, Y. Y. Lee, M. Kim, N. H. Cho, K. Chang, W. S. Kim, J. Rho and K. T. Nam, *Nature*, 2018, **556**, 360.

37 R. Zhu, H. Feng, Q. Li, L. Su, Q. Fu, J. Li, J. Song and H. Yang, *Angew. Chem., Int. Ed.*, 2021, **60**, 12560.

38 M. D. Malinsky, K. L. Kelly, G. C. Schatz and R. P. Van Duyne, *J. Am. Chem. Soc.*, 2001, **123**, 1471.

39 S. Hanif, H. Liu, M. Chen, P. Muhammad, Y. Zhou, J. Cao, S. A. Ahmed, J. Xu, X. Xia, H. Chen and K. Wang, *Anal. Chem.*, 2017, **89**, 2522.